

Auxiliary-field quantum Monte Carlo calculations with multiple-projector pseudopotentials

Fengjie Ma,^{*} Shiwei Zhang, and Henry Krakauer*Department of Physics, College of William and Mary, Williamsburg, Virginia 23187, USA*

(Received 19 October 2016; revised manuscript received 11 January 2017; published 4 April 2017)

We have implemented recently developed multiple-projector pseudopotentials into the plane-wave-based auxiliary-field quantum Monte Carlo (pw-AFQMC) method. Multiple-projector pseudopotentials can yield smaller plane-wave cutoffs while maintaining or improving transferability. This reduces the computational cost of pw-AFQMC, increasing its reach to larger and more complicated systems. We discuss the use of nonlocal pseudopotentials in the separable Kleinman-Bylander form, and the implementation in pw-AFQMC of the multiple-projector optimized norm-conserving pseudopotential ONCVSP of Hamann. The accuracy of the method is first demonstrated by equation-of-state calculations of the ionic insulator NaCl and more strongly correlated metal Cu. The method is then applied to calibrate the accuracy of density-functional theory (DFT) predictions of the phase stability of recently discovered high temperature and pressure superconducting sulfur hydride systems. We find that DFT results are in good agreement with pw-AFQMC, due to the near cancellation of electron-electron correlation effects between different structures.

DOI: [10.1103/PhysRevB.95.165103](https://doi.org/10.1103/PhysRevB.95.165103)

I. INTRODUCTION

The search for new materials and their development has increasingly relied on theoretical modeling. Methods based on density-functional theory (DFT) are efficient and powerful, but their predictions can break down in a number of instances. Examples range from strongly correlated materials, such as transition-metal systems, to bond stretching or bond breaking in otherwise moderately correlated systems. Explicit many-body methods, which avoid the mean-field-like approximations used in standard DFT calculations, are needed in these cases. Quantum Monte Carlo (QMC) calculations have become increasingly important in this regard because of their accuracy and favorable scaling (as a low-order polynomial of system size, similar to DFT, but with a larger prefactor) compared to traditional wave-function-based correlated methods. Routine applications of QMC calculations in extended systems still face major challenges, however.

In diffusion QMC (DMC) [1] and the plane-wave-based auxiliary-field quantum Monte Carlo method (pw-AFQMC) [2–5], pseudopotentials are usually used, except for some DMC calculations with the lightest elements. Pseudopotentials remove the chemically inactive core electrons, reducing the number of electrons that must be explicitly correlated and greatly reducing the computational cost. Nonlocal norm-conserving pseudopotentials (NCPPs) are typically used in QMC. The NCPPs are usually constructed from mean-field DFT or Hartree-Fock (HF) calculations. While computationally expedient, the transferability of NCPPs is a key issue, and the neglected core-core and core-valence correlation effects may need to be considered. Even setting these many-body effects aside, transferability errors from NCPPs in QMC calculations can be significant. In DMC, moreover, the nonlocality of NCPPs is handled with an additional locality approximation, whose accuracy depends on the quality of the

trial wave function [6]. The overall NCPP error can be significant compared to errors from the fixed-node approximation [7–9], which is used to control the fermion sign problem. In pw-AFQMC, nonlocal NCPPs can be used without additional approximations [2,3], but transferability errors can still be a problem, unless the NCPPs are made very hard [3–5,10], which requires large plane-wave cutoffs and increases the computational cost.

Pseudopotentials are based on the frozen-core approximation, but they contain an additional layer of approximation. Frozen-core calculations are common in quantum chemistry applications, where the core orbitals are frozen at the mean-field level derived from the *target* system. Pseudopotentials are usually constructed for a reference *atomic* configuration and then used in many target systems. The accuracy (transferability) of the PP across many target systems must then be determined *a posteriori*. In addition to being norm-conserving, most NCPPs used in QMC calculations are of single-projector type (one per angular momentum channel), which can further contribute to transferability errors.

Recently, Hamann proposed a multiple-projector pseudopotential [11], based on Vanderbilt's norm-conserving construction [12] and optimized with the Rappe-Rabe-Kaxiras-Joannopoulos pseudization scheme [13]. The resulting pseudopotential, referred to as ONCVSP by Hamann, was shown to have accuracy comparable to all-electron (AE) and ultrasoft pseudopotentials [12] (USPPs) in DFT calculations, with moderate plane-wave energy cutoffs. Schlipf and Gygi [14] recently presented a set of automatically constructed Hamann ONCVSPs for most of the Periodic Table. These were shown to be in good agreement with the all-electron results in DFT, often with cutoffs of only about 40 Ry [14,15]. The ONCVSP is of separable Kleinman-Bylander type [16], similar to NCPPs widely used in plane-wave DFT calculations and also in pw-AFQMC calculations. Since the treatment of one-particle Hamiltonian terms in pw-AFQMC is closely related to that in plane-wave DFT, the implementation of ONCVSP into our pw-AFQMC code is straightforward.

In this paper, we show that the use of multiple-projector ONCVSP can greatly reduce the plane-wave basis size

^{*}Present address: Center for Advanced Quantum Studies and Department of Physics, Beijing Normal University, Beijing 100875, China; fengjie.ma@bnu.edu.cn

in pw-AFQMC many-body calculations, while maintaining good accuracy. This results in significant reductions of computational cost, both by reducing the computing time for each step in the random walks and, at the same time, by reducing QMC statistical variance, due to the reduced number of AFQMC auxiliary fields. To test the new capability with multiple-projector ONCVSPs, we carry out pw-AFQMC calculations of the equation-of-state in the insulator NaCl and the transition metal solid Cu. We then study the high-pressure superconducting system H₃S, to calibrate DFT predictions of phase stabilities. Finally we discuss the performance of the DFT- or HF-generated pseudopotentials in many-body calculations and the difference from their use in DFT calculations.

The remainder of the paper is organized as follows. Section II reviews AFQMC with a plane-wave basis and pseudopotentials, and discusses the implementation of multiple-projector separable pseudopotentials in pw-AFQMC. Section III presents applications of the method. Additional transferability issues and other aspects of ONCVSP for many-body applications are discussed in Sec. IV. We then conclude with some general remarks in Sec. V.

II. PW-AFQMC METHODOLOGY

To set the context for the implementation of multiple-projector NCPPs in pw-AFQMC, we briefly review pertinent aspects of the formalism in this section. For more details about the pw-AFQMC method, see Refs. [2,3,10].

A. Hamiltonian

The electronic Hamiltonian within the Born-Oppenheimer approximation is

$$\hat{H} = \hat{K} + \hat{V}_{ee} + \hat{V}_{ei} + V_{ii}, \quad (1)$$

where \hat{K} , \hat{V}_{ee} , \hat{V}_{ei} , and V_{ii} are, respectively, the kinetic energy and electron-electron, electron-ion, and classical Coulomb ion-ion [17] interactions. The pseudopotential contributions appear in the electron-ion interaction \hat{V}_{ei} . With periodic boundary conditions and a plane-wave basis,

$$\langle \mathbf{r} | \mathbf{G} \rangle \equiv \langle \mathbf{r} | c_{\mathbf{G}}^\dagger | 0 \rangle = \frac{1}{\sqrt{\Omega}} \exp(i\mathbf{G} \cdot \mathbf{r}), \quad (2)$$

the terms in Eq. (1) can be expressed in second quantized form as

$$\hat{K} = \frac{1}{2} \sum_{\mathbf{G},s} G^2 c_{\mathbf{G},s}^\dagger c_{\mathbf{G},s}, \quad (3a)$$

$$\begin{aligned} \hat{V}_{ee} = & \frac{1}{2} N \xi + \frac{1}{2\Omega} \sum_{\mathbf{Q} \neq 0} \frac{4\pi}{Q^2} \hat{\rho}^\dagger(\mathbf{Q}) \hat{\rho}(\mathbf{Q}) \\ & - \frac{1}{2\Omega} \sum_s \sum_{\mathbf{G},\mathbf{G}'} \frac{4\pi}{|\mathbf{G} - \mathbf{G}'|^2} c_{\mathbf{G},s}^\dagger c_{\mathbf{G}',s}, \end{aligned} \quad (3b)$$

$$\begin{aligned} \hat{V}_{ei} = & \frac{1}{2} \sum_{\mathbf{Q} \neq 0} V_L(\mathbf{Q}) [\hat{\rho}(\mathbf{Q}) + \hat{\rho}^\dagger(\mathbf{Q})] \\ & + \sum_{\mathbf{G},\mathbf{G}'} V_{NL}(\mathbf{G},\mathbf{G}') c_{\mathbf{G}}^\dagger c_{\mathbf{G}'} + N V_L(\mathbf{0}). \end{aligned} \quad (3c)$$

Here, $c_{\mathbf{G}}^\dagger$ ($c_{\mathbf{G}}$) is a creation (destruction) operator, Ω is the volume of the simulation cell, \mathbf{G} is a reciprocal-lattice vector, $\mathbf{Q} = \mathbf{G}' - \mathbf{G}$, s is the electron spin, and N is the number of electrons in the simulation cell. Both \mathbf{G} and \mathbf{G}' belong to the plane-wave basis set $\{\mathbf{G}\}$ whose size is controlled by the plane-wave kinetic energy cutoff $E_{\text{cut}} \geq |\mathbf{G}|^2/2$. (When twist-averaged boundary conditions are used, \mathbf{G} is replaced by $\mathbf{k} + \mathbf{G}$, where \mathbf{k} is within the first Brillouin zone.) The constant ξ gives the self-interaction of an electron with its periodic images [18]. The one-body density operator $\hat{\rho}(\mathbf{Q})$ is given by

$$\hat{\rho}(\mathbf{Q}) \equiv \sum_{\mathbf{G},s} c_{\mathbf{G}+\mathbf{Q},s}^\dagger c_{\mathbf{G},s} \theta(E_{\text{cut}} - |\mathbf{G} + \mathbf{Q}|^2/2), \quad (4)$$

where the step function θ ensures that $(\mathbf{G} + \mathbf{Q})$, like \mathbf{G} , falls within the plane-wave basis set.

The local and nonlocal parts of the pseudopotential are defined by the plane-wave matrix elements $V_L(\mathbf{Q})$ and $V_{NL}(\mathbf{G},\mathbf{G}')$, respectively, which are discussed in more detail in Sec. II C.

B. Ground-state projection

AFQMC uses iterative imaginary-time projection to obtain the ground state $|\Psi_0\rangle$ from a trial wave function $|\Psi_T\rangle$ (often just a single Slater determinant):

$$e^{-\beta \hat{H}} |\Psi_T\rangle \rightarrow |\Psi_0\rangle \quad (\beta \rightarrow \infty), \quad (5)$$

where $\langle \Psi_T | \Psi_0 \rangle \neq 0$ is assumed. The projection is implemented as random walks in the space of Slater determinants. A key point in implementing this is the observation that a one-body propagator acting on a Slater determinant simply yields another Slater determinant. The AFQMC procedure is therefore to separate the propagator in Eq. (5) into one- and two-body propagators. This motivates the introduction of a small imaginary-time step $\Delta\tau$:

$$e^{-\Delta\tau \hat{H}} e^{-\Delta\tau \hat{H}} \dots e^{-\Delta\tau \hat{H}} |\Psi_T\rangle \rightarrow |\Psi_0\rangle. \quad (6)$$

A Trotter-Suzuki decomposition [19,20] then achieves the desired separation,

$$e^{-\Delta\tau \hat{H}} = e^{-\frac{1}{2}\Delta\tau \hat{H}^{(1)}} e^{-\Delta\tau \hat{H}^{(2)}} e^{-\frac{1}{2}\Delta\tau \hat{H}^{(1)}} + O(\Delta\tau^3), \quad (7)$$

where $\hat{H}^{(1)}$ and $\hat{H}^{(2)}$ are the one- and two-body parts of the Hamiltonian in Eq. (1), with $\hat{H}^{(2)} = 1/(2\Omega) \sum_{\mathbf{Q} \neq 0} \frac{4\pi}{Q^2} \hat{\rho}^\dagger(\mathbf{Q}) \hat{\rho}(\mathbf{Q})$ and $\hat{H}^{(1)}$ denoting the remaining terms in Eq. (3b) and the collection from Eqs. (3a) and (3c).

A Hubbard-Stratonovich transformation [21,22] allows one to express two-body propagators as a high-dimensional integral over auxiliary fields $\{\sigma_i\}$ of one-body propagators:

$$\begin{aligned} & \exp\left(-\frac{1}{2}\Delta\tau \sum_i \lambda_i \hat{b}_i^2\right) \\ & = \int \left(\prod_i \frac{d\sigma_i}{\sqrt{2\pi}}\right) \exp\left[\sum_i \left(-\frac{1}{2}\sigma_i^2 + \sigma_i \sqrt{-\Delta\tau \lambda_i} \hat{b}_i\right)\right], \end{aligned} \quad (8)$$

where the \hat{b}_i are any one-body operators. Applying this to $e^{-\Delta\tau\hat{H}^{(2)}}$ we have

$$e^{-\Delta\tau\hat{H}^{(2)}} = \left(\frac{1}{\sqrt{2\pi}}\right)^{D_\sigma} \int d\sigma e^{-(1/2)\sigma\cdot\sigma} e^{\sqrt{\Delta\tau}\sigma\cdot\hat{\mathbf{v}}}, \quad (9)$$

where we have introduced the vector of auxiliary fields $\sigma \equiv \{\sigma_i\}$, whose dimension, D_σ , is given by the number of possible \mathbf{Q} vectors. The operators $\hat{\mathbf{v}} \equiv \{\sqrt{-\lambda_i}\hat{b}_i\}$ are given by linear combinations of $\hat{\rho}^\dagger(\mathbf{Q})$ and $\hat{\rho}(\mathbf{Q})$ [2,3].

Our focus in this paper is on the choice of pseudopotentials, which appear only in the one-body propagator $e^{-\frac{1}{2}\Delta\tau\hat{H}^{(1)}}$. The handling of the two-body propagator and the implementation of the AFQMC phaseless approximation are unchanged from previous applications and can be found in Refs. [2,3,10].

The overall computing cost in QMC depends not only on the computer time to execute a single time step for each random walker, but also on the statistical variance, which controls the size of the Monte Carlo sampling required to achieve a targeted statistical uncertainty (the QMC efficiency) [5]. The computing cost to execute a single imaginary-time step [Eq. (6)] in pw-AFQMC is proportional to $M \ln(M)$, where $M \propto E_{\text{cut}}^{3/2}$ is the number of plane waves. [The overall scaling is $N^2 M \ln(M)$, where N is the number of electrons in the simulation cell.] The statistical variance depends on the number of auxiliary fields $D_\sigma \propto 8 E_{\text{cut}}^{3/2}$. Reducing E_{cut} can therefore both reduce the computing time for each step in the random walk and increase the QMC efficiency. Convergence with respect to E_{cut} is controlled by the pseudopotential hardness [2,3], so that soft accurate pseudopotentials can potentially lead to major improvements in pw-AFQMC.

C. Pseudopotential

The pseudopotential appears in the electron-ion interaction, $\hat{V}_{\text{ei}} = \hat{V}_{\text{L}} + \hat{V}_{\text{NL}}$ in Eq. (3c). In second-quantized form, the pseudopotential's action is safely isolated in the plane-wave matrix elements of its local $[V_{\text{L}}(\mathbf{Q})]$ and nonlocal $[V_{\text{NL}}(\mathbf{G}, \mathbf{G}')]^T$ parts, exactly as in DFT plane-wave methods [17]. Nonlocal potentials thus present no difficulties in AFQMC (unlike in the real-space-based DMC method [6]). The plane-wave matrix elements of the local part of the pseudopotential are given by

$$V_{\text{L}}(\mathbf{Q}) = \frac{1}{\Omega} \sum_{\alpha} e^{-i\mathbf{Q}\cdot\mathbf{d}_{\alpha}} V_{\alpha,\text{L}}(\mathbf{Q}), \quad (10)$$

where \mathbf{d}_{α} is the position of atom α in the simulation cell, and $V_{\alpha,\text{L}}(\mathbf{Q})$ is the Fourier transform of the (spherical) local part of the atomic pseudopotential. For single-projector NCPPs, the nonlocal part of the atomic pseudopotential is expressed by the separable Kleinman-Bylander [16] form,

$$\hat{V}_{\alpha,\text{NL}} = \sum_{m=-l}^l \frac{|V_{\alpha,l}^{\text{ps}} \varphi_{\alpha,l} Y_{lm}\rangle \langle Y_{lm} \varphi_{\alpha,l} V_{\alpha,l}^{\text{ps}}|}{\langle Y_{lm} \varphi_{\alpha,l} | V_{\alpha,l}^{\text{ps}} | \varphi_{\alpha,l} Y_{lm}\rangle}, \quad (11)$$

where, for each partial wave (e.g., $l = 0, 1, 2$ for 3d transition elements), there is only one projector. (The pseudopotential $V_{\alpha,l}^{\text{ps}}$ and pseudo-orbital $\varphi_{\alpha,l}$ are both functions of radial distance r only, and Y_{lm} is the usual spherical harmonic function.) The matrix elements $V_{\text{NL}}(\mathbf{G}, \mathbf{G}')$ of the nonlocal part of the pseudopotential can then be expressed in a separable

form as

$$V_{\text{NL}}(\mathbf{G}, \mathbf{G}') = \sum_{j \in \{\alpha, l, m\}} \frac{1}{\eta_j} F_j^*(\mathbf{G}) F_j(\mathbf{G}'), \quad (12)$$

where $\eta_j = \langle Y_{lm} \varphi_{\alpha,l} | V_{\alpha,l}^{\text{ps}} | \varphi_{\alpha,l} Y_{lm} \rangle$, and

$$F_j(\mathbf{G}) = \frac{4\pi}{\sqrt{\Omega}} e^{i\mathbf{G}\cdot\mathbf{d}_{\alpha}} f_{\alpha,l}(\mathbf{G}) Y_{lm}^*(\hat{\mathbf{G}}), \quad (13)$$

where $f_{\alpha,l}(\mathbf{G})$ is obtained from the Bessel transform of the projector $|V_{\alpha,l}^{\text{ps}} \varphi_{\alpha,l} Y_{lm}\rangle$. The separable form of $V_{\text{NL}}(\mathbf{G}, \mathbf{G}')$ greatly simplifies and speeds up the use of the NCPPs, just as in DFT methods.

Equation (11) can be abbreviated as $\hat{V}_{\alpha,l,\text{NL}} \equiv \frac{|\chi_l\rangle\langle\chi_l|}{b_l}$, in which b_l is the overlap between pseudo-wave-function $\phi_{\alpha,l}^{\text{ps}}$ with constructed projector $|\chi\rangle = V_{\alpha,l}^{\text{ps}} |\phi_{\alpha,l}^{\text{ps}}\rangle$. Having only one projector for each partial wave l limits the energy range over which an NCPP can reproduce the scattering properties of the all-electron potential, which reduces its transferability. Hamann generalized Eq. (11) for optimized multiple projectors (in practice, implemented for two projectors per partial wave) [11]. Written in a diagonal representation, the multiple-projector pseudopotential can be compactly expressed for atom α and partial wave l as [11]

$$\hat{V}_{\alpha,l,\text{NL}} = \sum_{i=1}^2 \frac{|\chi_i\rangle\langle\chi_i|}{b_i}. \quad (14)$$

Implementing the ONCVSP in this form requires only minor modifications in pw-AFQMC, compared to Eq. (11). The extended energy range over which the scattering properties are reproduced often allows a smaller plane wave E_{cut} with excellent transferability properties [11].

III. APPLICATIONS

We describe applications of pw-AFQMC with ONCVSP in three systems, the ionic insulator NaCl, the strongly correlated metal Cu, and the recently discovered sulfur hydride high- T_c and high-pressure superconductors.

A. Ionic insulator: NaCl

NaCl is a typical ionic compound, which crystallizes in the fcc structure. Due to the large overlap of Na valence 3s electron and semicore 2s and 2p states, care must be used in the choice of pseudopotentials. Relaxation of the semicore states can significantly affect valence electron and hence material properties. Neglecting these effects, for example, by treating the 2s and 2p electrons as core states will give $\sim 10\%$ underestimation of the lattice constant and 45% overestimation of the bulk modulus of Na in DFT calculations. Pseudizing instead the 2s and 2p states greatly reduces the discrepancy in the lattice constant to $\sim 1.6\%$ using the local-density approximation (LDA) exchange-correlation functional. Calculated equations of state (EOSs) with the LDA pseudopotentials are shown in Fig. 1. ONCVSP results are compared to those from the all-electron linearized augmented plane wave (LAPW) and the projector augmented wave (PAW) methods, using ELK [24] and ABINIT [25], respectively. ONCVSPs were generated with Hamann's open source

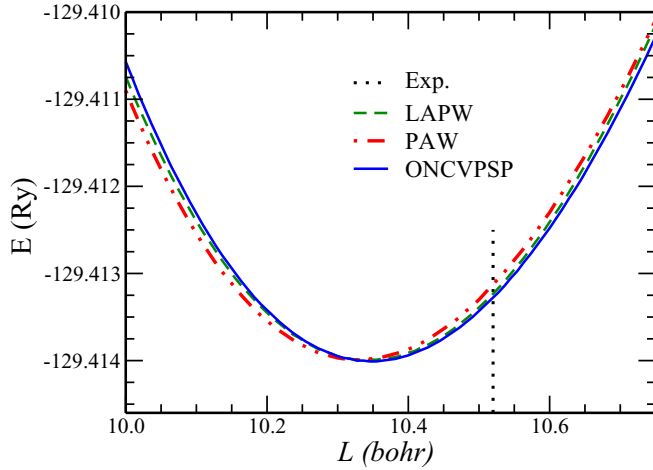


FIG. 1. NaCl DFT/LDA calculated EOS curves (fits to Murnaghan's equation [23]), comparing all-electron LAPW (green dashed line), PAW (red dot-dashed line), and ONCVSP (blue solid line). Curves are shifted to have the same minimum energy. The experimental lattice constant is indicated by the black dotted vertical line.

pseudopotential code [26]. Both ONCVSP and PAW results are in excellent agreement with LAPW. The agreement can be further quantified using the Δ factor, which was recently introduced by Lejaeghere *et al.* [27] for comparing two EOS curves, $E_1(V)$ and $E_2(V)$. Aligning the minimum energies, the definition of Δ is

$$\Delta = \sqrt{\frac{\int [E_2(V) - E_1(V)]^2 dV}{\Delta V}} \quad (15)$$

for a volume range ΔV . (A typical choice of ΔV is $\pm 6\%$ around the equilibrium volume.) The Δ factors are 0.89 and 0.79 meV for ONCVSP and PAW calculations, respectively. The Na and Cl multiple-projector ONCVSP pseudopotentials required kinetic energy cutoffs of only $E_{\text{cut}} = 40$ Ry, much softer than for a single-projector norm-conserving pseudopotentials, which would have required $E_{\text{cut}} = 100$ Ry.

Figure 2 shows the calculated pw-AFQMC NaCl EOS. A four-formula cubic simulation cell was used with a twist boundary condition corresponding to the L special \mathbf{k} -point (0.5, 0.5, 0.5); one- and two-body finite-size errors were reduced, using a postprocessing finite-size correction scheme [28,29]. Here and throughout the rest of this paper, Trotter errors from Eq. (7) are removed by either extrapolation to the $\Delta\tau = 0$ limit or choosing sufficiently small time-step values. Our pw-AFQMC calculations used LDA-generated trial wave functions. The discrepancy of DFT/LDA with experiment is essentially eliminated by the many-body calculations. The equilibrium lattice constant and bulk modulus calculated from pw-AFQMC, $a_0 = 10.48(3)$ bohr and $B_0 = 26(2)$ GPa, are in excellent agreement with the experimental values, $a_0 = 10.52$ bohr and $B_0 = 26.6$ GPa [30].

B. Transition metal: fcc Cu

Transition-metal materials have played a central role in the study of strongly correlated physics, and copper-based systems

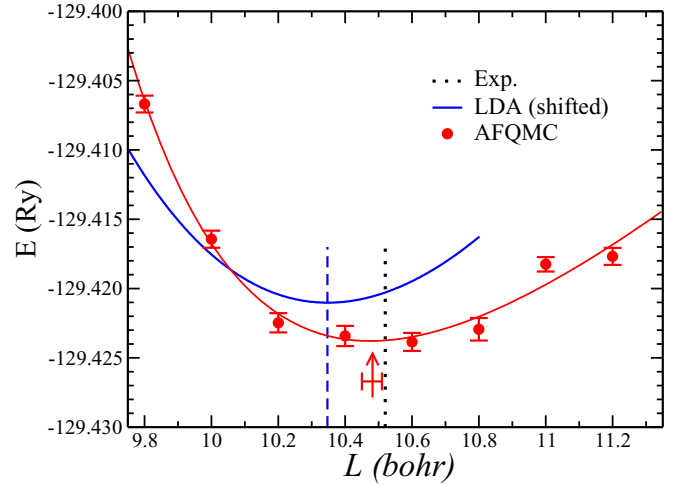


FIG. 2. NaCl EOS calculated from pw-AFQMC (filled red circles with statistical error bars) using the same ONCVSPs as in Fig. 1. For comparison, the DFT EOS in Fig. 1 is reproduced (blue solid line, energy shifted for convenient display). The vertical blue dashed and black dotted lines indicate the DFT and experimental equilibrium lattice constants a_0 , respectively. The pw-AFQMC calculated a_0 is indicated by the vertical red arrow, with a horizontal error bar indicating the uncertainty from a fit of the statistical data to Murnaghan's equation [23].

in particular have attracted a great deal of attention [31]. *Ab-initio* many-body calculations for transition-metal systems have been very limited [32], and most previous calculations have relied on DFT or related approaches. In this subsection, we present many-body pw-AFQMC results on fcc copper, a prototypical correlated metal.

For good transferability, a frozen neon-core Cu pseudopotential is required, retaining the $3s^2 3p^6 3d^{10} 4s^1$ states. Single-projector NCPPs are challenged in this regard, because the $l = 0$ and 1 scattering properties near the Fermi energy E_F depend on projectors constructed at much lower energies from the semicore $3s$ and $3p$ states. Even the $l = 2$ scattering properties near E_F are difficult, due to the resonant nature of $3d$ scattering. To maximize the accuracy, very hard single-projector NCPPs must be used, with large plane wave $E_{\text{cut}} \sim 200$ Ry. This is alleviated by the multiple-projector ONCVSP. Projectors for $l = 0$ and 1 can be constructed using both the semicore $3s$ and $3p$ and higher-lying valence or virtual $4s$ and $4p$ states. Similarly, two reference energies can be used to closely reproduce the all-electron $l = 2$ scattering. We used $E_{\text{cut}} = 64$ Ry and radial cutoffs [11] of $r_c = 1.60, 1.97$, and 1.97 bohr for $l = 0, 1$, and 2 , respectively. The projectors were constructed using the ONCVSP code [26], with the LDA exchange-correlation functional. The multiple-projector pseudopotential yields very good agreement with all-electron LAPW results at the DFT level, giving a Δ factor ~ 1.6 meV, as shown in Fig. 3. The nonparallelity error of ~ 1 mRy in the computed EOS is smaller than the targeted statistical resolution of the QMC calculations, which we discuss next.

Figure 4 shows the calculated pw-AFQMC Cu EOS. A four-atom cubic simulation cell was used. Because Cu is metallic, twist-averaging with a $6 \times 6 \times 6$ Monkhorst-Pack (MP) \mathbf{k} -point grid [33] was applied. Small random distortions

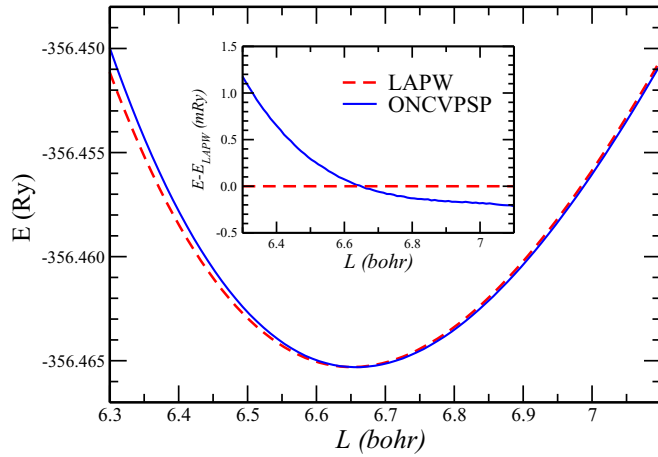


FIG. 3. Cu DFT/LDA EOS comparison of ONCVSP and LAPW. The EOSs are shifted to have the same minimum energy. The inset shows the energy difference vs lattice size.

were applied to each of the \mathbf{k} points to lift band degeneracy in the trial wave function. Additionally, postprocessing one- and two-body finite-size error corrections [28,29] were applied. The residual finite-size error is not expected to affect the EOS around equilibrium significantly. This was verified with the following approximate estimate, which helps to avoid many computationally costly QMC tests. Calculations with up to $4 \times 4 \times 4$ of a primitive unit cell were carried out using the LDA+ U method. The DFT+ U method includes a mean-field treatment of on-site $3d$ electron-electron interactions on the Cu atoms. This effect is absent in standard DFT local and semilocal exchange-correlation functionals, which are based on electron gas calculations. Since the choice of U is largely

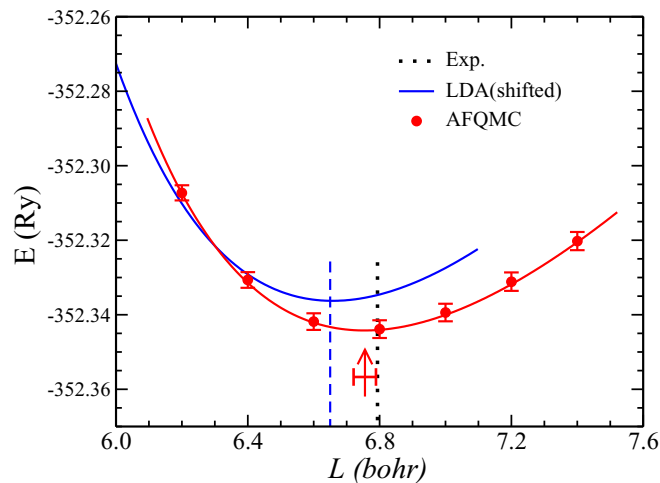


FIG. 4. Cu EOS calculated by pw-AFQMC using the same ONCVSP as in Fig. 3. AFQMC results are shown by filled symbols, with statistical error bars indicated. For comparison, the DFT EOS with ONCVSP is reproduced from Fig. 3 (blue solid line, energy shifted). The vertical blue dashed and black dotted lines indicate the DFT and experimental equilibrium lattice constants a_0 , respectively. The pw-AFQMC calculated a_0 is indicated by the vertical red arrow, with a horizontal error bar indicating the uncertainty from a fit to Murnaghan's equation [23].

determined by experience and by systematic benchmarking, multiple effective values of U , from 0.001 to 5.0, are studied in the simulations. The same twist-averaging and postprocessing finite-size techniques were applied to the LDA+ U results. The equilibrium lattice constant and bulk modulus did not change up to the largest test simulation cells. The final calculated pw-AFQMC EOS in Fig. 4 yields an equilibrium lattice constant and bulk modulus, $a_0 = 6.76(3)$ bohr and $B_0 = 155(13)$ GPa, which are in excellent agreement with experimental values $a_0 = 6.79$ bohr and $B_0 = 145$ GPa (zero-point effects removed) [30]. The accuracy of the ONCVSP compared to all-electron LAPW results at the DFT level, without partial core corrections (see Sec. IV), is thus seen to be a good predictor of its transferability at the pw-AFQMC many-body level.

C. Sulfur hydride high- T_c high-pressure superconductor: H_3S

In this subsection, we present benchmark pw-AFQMC calculations on two candidate structures for high-temperature, high-pressure superconductivity in the sulfur hydride system. Applying the multiple-projector pseudopotentials, we test DFT/GGA predictions of the structural energetics of H_2S and H_3S by comparison with many-body AFQMC results.

Since Ashcroft proposed that metallic hydrogen should exhibit superconductivity with $T_c \sim 270$ K [34], there have been many investigations of prospective high- T_c materials incorporating hydrogen, with a recent focus on hydrides, where reduced metallization pressures are expected [35]. Recent theoretical predictions [36,37] of unusually high T_c in sulfur hydrides under high pressure were subsequently supported by experiment [38–40]. Measurements of resistivity and magnetic susceptibility indicate superconducting temperatures as high as $T_c = 203$ K at pressures ~ 150 GPa [38]; this was attributed to the $Im\bar{3}m$ H_3S phase. A novel experiment reported Meissner effect measurements that qualitatively confirmed the finding [39]. Subsequent DFT-based calculations have led to similar conclusions regarding the central role of electron-phonon coupling in driving the superconducting transition [41–45]. These calculations support the view that the sulfur hydrides are conventional superconductors, which are well described by Bardeen-Cooper-Schrieffer (BCS) theory [46] with strong electron-phonon coupling leading to high T_c . This is unlike the previously known high- T_c cuprate and iron-based superconductors, where strong electron-electron interactions are believed to play a key role, although the superconducting mechanism has not yet been established. With $T_c \sim 203$ K [38], hydrogen sulfide is one of the highest temperature superconductors on record, although extremely high pressures are required. Their discovery has reenergized the search for new superconductors in hydrogen-based and related materials.

Little is known experimentally regarding the high-pressure stability of hydrogen sulfide compounds. There has therefore been a strong reliance on standard DFT calculations, which have examined the high-pressure phase stabilities and structures of H_nS [41,42,44]. The H_3S $Im\bar{3}m$ structure (space group No. 229) has been a leading candidate for the stoichiometry that leads to the highest T_c . Other stoichiometries such as H_2S are predicted to have competitive but less favorable enthalpies. It is important, therefore, to test these predictions

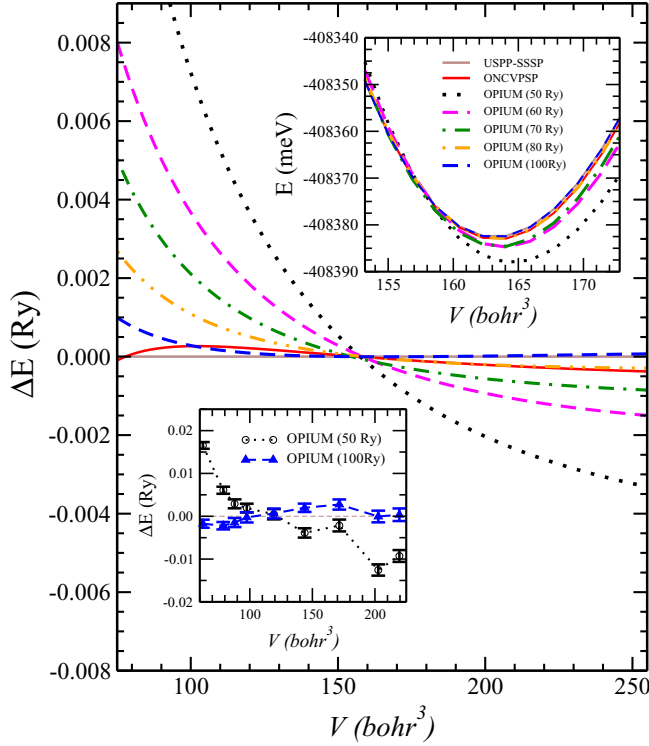


FIG. 5. H_3S ($Im\bar{3}m$) EOS calculated with ONCVSPSP, single-projector NCPP, and USPP pseudopotentials, plotted as $\Delta E(V) = E(V) - E_{\text{USPP}}$ (minimum energies aligned). OPIUM generated NCPP EOS are shown for a range of E_{cut} . The upper-right inset shows the actual EOS. Raw AFQMC results with OPIUM 50 and 100 Ry pseudopotentials are plotted in the lower-left inset, using ONCVSPSP results as reference.

with accurate many-body calculations. Here, we focus on candidate structures for two compositions, H_2S and H_3S , and we compare the pw-AFQMC results of their structural energetics with DFT/GGA predictions.

The ONCVSPSPs of H and S were generated with $E_{\text{cut}} = 50$ Ry. The $l = 2$ projectors for S used unbound scattering states [11,12]. Figure 5 compares calculated ONCVSPSP EOS with ultrasoft (USPP) and single-projector NCPP pseudopotential calculations, using the DFT GGA/PBE xc functional. The NCPPs were generated with the OPIUM [47] package for several values of E_{cut} , and USPP standard solid-state pseudopotentials (USPP-SSSP) are adopted [15]. ONCVSPSP is in excellent agreement with USPP over a wide volume range (~ 75 – 255 bohr^3). The difference is less than 0.5 mRy per formula unit. Using USPP-SSSP as the reference, Δ is 0.6 meV for ONCVSPSP over the typical choice of ΔV , $\pm 6\%$ around the equilibrium volume of $V_0 \simeq 163$ bohr^3 . The volume range in Fig. 5 of 75 – 255 bohr^3 is much wider, covering a $\pm 50\%$ span and including the superconducting volume near 90 bohr^3 at a transition pressure 200 GPa. For this volume range, the Δ is 3.0 meV for ONCVSPSP. By comparison, the single-projector NCPPs have Δ values of 68.1, 34.6, 20.7, 10.6, and 3.4 meV for E_{cut} values of 50, 60, 70, 80, and 100 Ry, respectively. To achieve comparable accuracy with the ONCVSPSP, the NCPP requires a $E_{\text{cut}} = 100$ Ry, which gives a nearly three times larger plane-wave basis.

TABLE I. Calculated pw-AFQMC structural energy difference for H_2S and H_3S , using ONCVSPSP, compared to DFT-based calculations for four functionals and three pseudopotentials. For each of the four crystal structures, the fully relaxed $P = 200$ GPa structure from ONCVSPSP-PBE was used for the pw-AFQMC calculations and for the other DFT functionals and pseudopotentials.

		H_2S	H_3S
		$E_{64} - E_{26}$	$E_{229} - E_{66}$
		(eV/at.)	(eV/at.)
AFQMC		$-0.086(7)$	$0.111(5)$
	ONCVSPSP	-0.082	0.058
LDA	OPIUM (100 Ry)	-0.083	0.056
	USPP	-0.084	0.056
	ONCVSPSP	-0.086	0.082
PBE	OPIUM (100 Ry)	-0.088	0.080
	USPP	-0.086	0.080
	ONCVSPSP	-0.083	0.060
PBEsol	OPIUM (100 Ry)	-0.084	0.058
	USPP	-0.084	0.059
PBE0	ONCVSPSP	-0.082	0.077

Before discussing AFQMC results for these systems, we present another benchmark of the ONCVSPSP multiple-projector pseudopotential we use. In Fig. 5 we show the EOS from AFQMC in a small cell, using both the ONCVSPSP and two single-projector pseudopotentials, one with E_{cut} of 100 Ry and the other 50 Ry. No finite-size corrections are applied. The calculated EOSs are compared directly after a constant overall shift in the energy is applied to align the curves. (The shift is obtained by setting to zero the average of the energy difference from the ONCVSPSP reference.) It is seen that, similar to the DFT calculations, a single-projector pseudopotential of $E_{\text{cut}} = 50$ Ry shows significant discrepancies with the ONCVSPSP. A harder pseudopotential of $E_{\text{cut}} = 100$ Ry is required to achieve good agreement.

For the pw-AFQMC benchmarks, we selected 200 GPa structures for two compositions, guided by the DFT/PBE results of Mazin *et al.* [41]. For H_2S , the space group structures $Pmc2_1$ (no. 26) and $Cmca$ (no. 64) were selected, both with 12-atom primitive cells. For H_3S , the space group structures $Cccm$ (no. 66) and $Im\bar{3}m$ (no. 229) were selected, with 32- and 4-atom primitive cells, respectively. We first calculated DFT-based energy differences $E_{64} - E_{26}$ for H_2S and $E_{229} - E_{66}$ for H_3S . Our ONCVSPSP DFT/PBE calculations are in very good agreement with the results in Ref. [41]. DFT-based results are shown in Table I for combinations of three pseudopotentials (ONCVSPSP, NCPP-100 Ry, and USPP) and four DFT exchange-correlation functionals: LDA, PBE, PBEsol, and the hybrid PBE0 method. (Note that the sign of the energy differences does not reflect the relative structural stabilities. For example, the calculated H_3S DFT/PBE enthalpy is actually lowest [41], making it the most stable structure at $P = 200$ GPa.) To facilitate comparisons, the fully relaxed 200 GPa crystal structure from ONCVSPSP-PBE was used for the other functionals and pseudopotentials and for the pw-AFQMC calculations. For H_2S , $E_{64} - E_{26}$ is nearly independent of the choice of DFT functional, while for H_3S , $E_{229} - E_{66}$ varies between 0.056 to 0.082 eV/at.

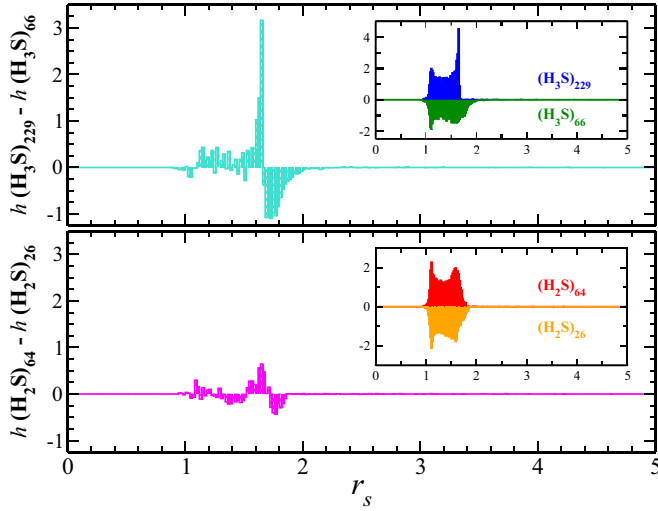


FIG. 6. Electron density distributions in H_3S (top panel) and H_2S (bottom panel) as a function of r_s , computed from DFT/PBE with ONCVSP. The main plots show the difference between the two space group structures for each composition, while the insets show the actual distributions of the two structures, with one shown as negative. $\Delta r_s = 0.02$ is chosen as the size of histogram bin.

For the pw-AFQMC calculations, 24-atom simulation cells were used for H_2S , doubling the size of the primitive unit cell in each structure. For H_3S , 32-atom simulation cells were used ($2 \times 2 \times 2$ for $Im\bar{3}m$). Twist-averaged boundary conditions with a $4 \times 4 \times 4$ MP grid were used. One- and two-body finite-size corrections [28,29] were then applied to the many-body results. The pw-AFQMC energy differences are also shown in Table I. The pw-AFQMC H_3S energy difference, 0.111(5) eV/at, is nearly twice that given by the LDA and PBEsol, and about 50% larger than those from PBE and PBE0, while in H_2S the DFT-based calculations are identical with pw-AFQMC to within its statistical uncertainty.

To understand how the better agreement in H_2S arises compared to H_3S , we investigated the electron-density distributions for each composition. The result is illustrated in Fig. 6, which plots the densities calculated from ONCVSP DFT/PBE for the four structures on the real-space FFT grid. In both H_3S and H_2S , the distribution is largely concentrated in the high-density region $r_s = 1-2$. The H_3S composition structures, however, show larger differences, especially in the range $r_s = 1.6-2.0$, than for the two H_2S structures. This provides a possible explanation of the better agreement of the different DFT functionals for H_2S than for H_3S . Similarly, it indicates that there will be better cancellation of electron correlation effects in H_2S , resulting in better agreement between DFT and pw-AFQMC many-body results.

The pw-AFQMC benchmarks in Table I show that DFT-based predictions are semiquantitatively correct. The DFT predictions of H_2S and H_3S enthalpy differences could be off by the order of 30 and 50 meV in PBE and PBEsol, respectively. However, the stabilities are dominated by independent-electron contributions to the enthalpy, which are significantly larger than these differences. This suggests that the predictions on phase stabilities and structures from recent DFT studies are likely reasonable.

IV. DISCUSSION

The applications above show that the use of a multiple-projector ONCVSP can greatly reduce the plane-wave basis size in pw-AFQMC many-body calculations, while maintaining or improving accuracy compared to single-projector NCPPs. ONCVSP uses two projectors per partial wave in our applications, which maintains fidelity to scattering properties at reduced E_{cut} . As discussed in Sec. II B, this results in significant reductions of the computational cost, both by reducing the computing time for each step in the random walk and, at the same time, increasing the QMC efficiency because of a smaller number of auxiliary fields in Eq. (8). For example, accurate results were obtained in fcc Cu with $E_{\text{cut}} = 64$ Ry, in contrast to an estimated value of $E_{\text{cut}} \sim 200$ Ry with NCPP.

It is important to note, however, that improvement in performance in DFT calculations by the ONCVSP over single-projector NCPP does not always correlate with improvement in QMC. There are fundamental differences in the role of DFT-generated pseudopotentials when applied in a many-body context, versus in DFT. Clearly, when core-valence (or core-core) correlation effects are non-negligible, the use of pseudopotentials generated from an independent-electron approach can incur errors in many-body calculations. This is not the case for the systems treated in this paper. For example, in NaCl, small-core pseudopotentials are taken to pseudize the $2s$ and $2p$ states in both DFT and AFQMC. In DFT, partial-core effects were negligible as shown by the good agreement with LAPW in Fig. 1. Similarly in AFQMC, excellent agreement is found with experiment in Fig. 2.

A good indicator of the accuracy of ONCVSPs in many-body calculations is good core-valence separation and good DFT performance of ONCVSP (without partial-core corrections) compared to all-electron calculations. The improved ONCVSP scattering properties and transferability then allow smaller values of E_{cut} , which can significantly reduce the many-body computing cost while retaining high accuracy. In intermediate cases, such as in Si, when partial-core corrections are necessary in DFT calculations, more care is required. (See the Appendix for an example in Si that illustrates the difference in pseudopotential accuracy between DFT and many-body situations.)

V. SUMMARY

We have successfully implemented the multiple-projector ONCVSP into the many-body pw-AFQMC method. The accuracy is demonstrated by calculations of bulk properties of NaCl and the more strongly correlated fcc Cu. With this technique, we also benchmarked the structure transition energy barriers in the recently discovered high-temperature superconductor sulfur hydride systems. In these systems, modest electron-electron correlation and large cancellation effects are seen in the energies between different structures, and we find that the estimations from DFT are in reasonable agreement with the many-body AFQMC results. The implementation of a multiple-projectors pseudopotential allows pw-AFQMC to treat systems with smaller pseudopotential errors and at significantly lower plane-wave-energy cutoffs, and hence to reach larger and more complicated systems.

ACKNOWLEDGMENTS

This work is supported by the DOE (Contract No. DE-SC0001303), the NSF (Grant No. DMR-1409510), and the ONR (Contract No. N000141211042). An award of computer time was provided by the Innovative and Novel Computational Impact on Theory and Experiment (INCITE) program, using resources of the Oak Ridge Leadership Computing Facility at the Oak Ridge National Laboratory, which is supported by the Office of Science of the U.S. Department of Energy under Contract No. DE-AC05-00OR22725. We also acknowledge computing support from the computational facilities at the College of William and Mary.

APPENDIX

A case that illustrates the difference in pseudopotential accuracy between DFT and many-body situations is bulk Si, where the Ne-core NCPP causes a pseudopotential error both in DFT and AFQMC. In DFT, this can be remedied using a partial-core correction, which is not available in AFQMC. One way to remove the Ne-core error in AFQMC is with the frozen-core (FC) approximation [4,5]. A He-core pseudopotential is used to generate DFT $2s$ and $2p$ orbitals in the crystalline solid environment. After a unitary rotation to the Kohn-Sham basis, the $2s$ and $2p$ orbitals are frozen [5]. The corresponding FC Hamiltonian, which incorporates an effective Ne-core pseudopotential, was shown to yield excellent results [5] (to generate the FC $2s$ and $2p$ orbitals and Kohn-Sham basis, the DFT calculation used an extremely high $E_{\text{cut}} \simeq 600$ Ry He-core NCPP). To further study the implicit treatment of core-valence interactions in the FC approximation, we repeated this procedure with a much softer He-core ONCVSP (~ 64 Ry). At the DFT level, this ONCVSP works as well as the 600 Ry NCPP. They both capture (treating 12 electrons/Si) the core-valence corrections and yield excellent agreement with all-electron LAPW and with partial-core-corrected Ne-core pseudopotential calculations. However, the corresponding FC AFQMC calculation is not improved, and a pseudopotential error is seen as in the Ne-core calculation.

These results are illustrated in detail in Fig. 7. The multiple-projectors ONCVSP with $E_{\text{cut}} = 64$ Ry, another ONCVSP with $E_{\text{cut}} = 200$ Ry, and the single-projector NCPP with $E_{\text{cut}} = 600$ Ry all yield excellent agreement with all-electron LAPW in DFT calculations. However, the corresponding

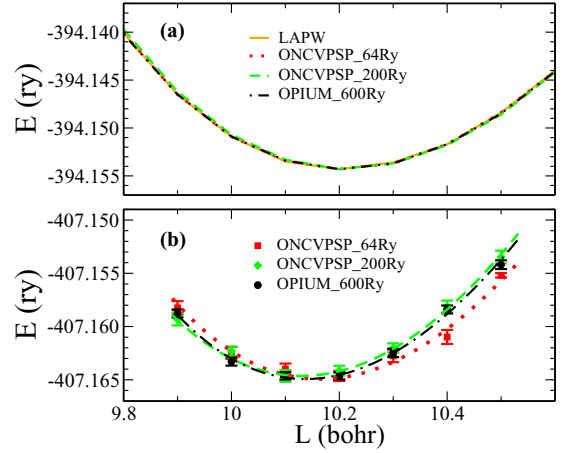


FIG. 7. Comparison of pseudopotentials in (a) DFT and (b) AFQMC FC calculations. Two multiple-projectors ONCVSPs with $E_{\text{cut}} = 64$ and 200 Ry and one single-projector NCPP with $E_{\text{cut}} = 600$ Ry are adopted. Finite-size correction is not included in the AFQMC results.

FC AFQMC calculations show a different behavior. The $E_{\text{cut}} = 64$ Ry ONCVSP shows substantial errors in the FC QMC calculation. The $E_{\text{cut}} = 200$ Ry ONCVSP is required to achieve the correct result in QMC.

The different behaviors in DFT and AFQMC/FC reflect the fundamental difference in the role of DFT-generated pseudopotentials when applied in a many-body context, versus in DFT. The softer $E_{\text{cut}} = 64$ Ry ONCVSP has a larger pseudizing radius, r_c . For $r < r_c$, the $2s$ and $2p$ pseudized orbitals are not faithful to the true orbitals. In DFT, such errors can be partially recovered, because the densities are properly compensated for. In QMC, however, when the less accurate $2s$ and $2p$ orbitals are frozen (treated at the mean-field level), the errors propagate into the FC many-body Hamiltonian that QMC treats, and these errors cannot be corrected. For the harder $E_{\text{cut}} = 200$ Ry ONCVSP, r_c is reduced, so the small- r accuracy of the $2s$ and $2p$ orbitals is improved, and it agrees very well with the hardest pseudopotential ($E_{\text{cut}} = 600$ Ry) [48]. This example illustrates the special attention that is required in many-body FC calculations for atoms where core-valence interactions are significant.

-
- [1] W. M. C. Foulkes, L. Mitas, R. J. Needs, and G. Rajagopal, *Rev. Mod. Phys.* **73**, 33 (2001).
 - [2] S. Zhang and H. Krakauer, *Phys. Rev. Lett.* **90**, 136401 (2003).
 - [3] M. Suewattana, W. Purwanto, S. Zhang, H. Krakauer, and E. J. Walter, *Phys. Rev. B* **75**, 245123 (2007).
 - [4] W. Purwanto, S. Zhang, and H. Krakauer, *J. Chem. Theory Comput.* **9**, 4825 (2013).
 - [5] F. Ma, W. Purwanto, S. Zhang, and H. Krakauer, *Phys. Rev. Lett.* **114**, 226401 (2015).
 - [6] L. Mitas, E. L. Shirley, and D. M. Ceperley, *J. Chem. Phys.* **95**, 3467 (1991).
 - [7] R. G. Hennig, A. Wadehra, K. P. Driver, W. D. Parker, C. J. Umrigar, and J. W. Wilkins, *Phys. Rev. B* **82**, 014101 (2010).
 - [8] S. Sorella, M. Casula, L. Spanu, and A. Dal Corso, *Phys. Rev. B* **83**, 075119 (2011).
 - [9] R. Nazarov, L. Shulenburger, M. Morales, and R. Q. Hood, *Phys. Rev. B* **93**, 094111 (2016).
 - [10] W. Purwanto, H. Krakauer, and S. Zhang, *Phys. Rev. B* **80**, 214116 (2009).
 - [11] D. R. Hamann, *Phys. Rev. B* **88**, 085117 (2013).
 - [12] D. Vanderbilt, *Phys. Rev. B* **41**, 7892 (1990).
 - [13] A. M. Rappe, K. M. Rabe, E. Kaxiras, and J. D. Joannopoulos, *Phys. Rev. B* **41**, 1227 (1990).

- [14] M. Schlipf and F. Gygi, *Comput. Phys. Commun.* **196**, 36 (2015).
- [15] K. Lejaeghere, G. Bihlmayer, T. Björkman, P. Blaha, S. Blügel, V. Blum, D. Caliste, I. E. Castelli, S. J. Clark, A. Dal Corso *et al.*, *Science* **351**, aad3000 (2016).
- [16] L. Kleinman and D. M. Bylander, *Phys. Rev. Lett.* **48**, 1425 (1982).
- [17] M. T. Yin and M. L. Cohen, *Phys. Rev. B* **26**, 3259 (1982).
- [18] L. M. Fraser, W. M. C. Foulkes, G. Rajagopal, R. J. Needs, S. D. Kenny, and A. J. Williamson, *Phys. Rev. B* **53**, 1814 (1996).
- [19] H. F. Trotter, *Proc. Am. Math. Soc.* **10**, 545 (1959).
- [20] M. Suzuki, *Commun. Math. Phys.* **51**, 183 (1976).
- [21] J. Hubbard, *Phys. Rev. Lett.* **3**, 77 (1959).
- [22] R. L. Stratonovich, *Sov. Phys. Dokl.* **2**, 416 (1957).
- [23] F. D. Murnaghan, *Proc. Natl. Acad. Sci. USA* **30**, 244 (1944).
- [24] The Elk full-potential linearized augmented-plane wave, available at <http://elk.sourceforge.net> (accessed May 1, 2011).
- [25] X. Gonze, J.-M. Beuken, R. Caracas, F. Detraux, M. Fuchs, G.-M. Rignanese, L. Sindic, M. Verstraete, G. Zerah, F. Jollet *et al.*, *Comput. Mater. Sci.* **25**, 478 (2002).
- [26] D. R. Hamann, Open-source pseudopotential code ONCVSP, available at <http://www.mat-simresearch.com/>.
- [27] K. Lejaeghere, V. V. Speybroeck, G. V. Oost, and S. Cottenier, *Crit. Rev. Solid State Mater. Sci.* **39**, 1 (2014).
- [28] H. Kwee, S. Zhang, and H. Krakauer, *Phys. Rev. Lett.* **100**, 126404 (2008).
- [29] F. Ma, S. Zhang, and H. Krakauer, *Phys. Rev. B* **84**, 155130 (2011).
- [30] L. Schimka, J. Harl, and G. Kresse, *J. Chem. Phys.* **134**, 024116 (2011).
- [31] W. E. Pickett, *Rev. Mod. Phys.* **61**, 433 (1989).
- [32] K. Foyevtsova, J. T. Krogel, J. Kim, P. R. C. Kent, E. Dagotto, and F. A. Reboredo, *Phys. Rev. X* **4**, 031003 (2014).
- [33] H. J. Monkhorst and J. D. Pack, *Phys. Rev. B* **13**, 5188 (1976).
- [34] N. W. Ashcroft, *Phys. Rev. Lett.* **21**, 1748 (1968).
- [35] N. W. Ashcroft, *Phys. Rev. Lett.* **92**, 187002 (2004).
- [36] Y. Li, J. Hao, H. Liu, Y. Li, and Y. Ma, *J. Chem. Phys.* **140**, 174712 (2014).
- [37] D. Duan, Y. Liu, F. Tian, D. Li, X. Huang, Z. Zhao, H. Yu, B. Liu, W. Tian, and T. Cui, *Sci. Rep.* **4**, 6968 (2014).
- [38] A. P. Drozdov, M. I. Eremets, I. A. Troyan, V. Ksenofontov, and S. I. Shylin, *Nature (London)* **525**, 73 (2015).
- [39] I. Troyan, A. Gavriluk, R. Rüffer, A. Chumakov, A. Mironovich, I. Lyubutin, D. Perekalin, A. P. Drozdov, and M. I. Eremets, *Science (New York, NY)* **351**, 1303 (2016).
- [40] M. Einaga, M. Sakata, T. Ishikawa, K. Shimizu, M. I. Eremets, A. P. Drozdov, I. A. Troyan, N. Hirao, and Y. Ohishi, *Nat. Phys.* **12**, 835 (2016).
- [41] N. Bernstein, C. S. Hellberg, M. D. Johannes, I. I. Mazin, and M. J. Mehl, *Phys. Rev. B* **91**, 060511 (2015).
- [42] D. Duan, X. Huang, F. Tian, D. Li, H. Yu, Y. Liu, Y. Ma, B. Liu, and T. Cui, *Phys. Rev. B* **91**, 180502 (2015).
- [43] D. A. Papaconstantopoulos, B. M. Klein, M. J. Mehl, and W. E. Pickett, *Phys. Rev. B* **91**, 184511 (2015).
- [44] I. Errea, M. Calandra, C. J. Pickard, J. Nelson, R. J. Needs, Y. Li, H. Liu, Y. Zhang, Y. Ma, and F. Mauri, *Phys. Rev. Lett.* **114**, 157004 (2015).
- [45] M. Komelj and H. Krakauer, *Phys. Rev. B* **92**, 205125 (2015).
- [46] J. Bardeen, L. N. Cooper, and J. R. Schrieffer, *Phys. Rev.* **108**, 1175 (1957).
- [47] E. J. Walter, OPIUM: Pseudopotential generation project, <http://opium.sourceforge.net>.
- [48] The radial cutoffs used for s , p , and d channels in the generated Si pseudopotentials, OPIUM 600 Ry, ONCVSP 200 Ry, and ONCVSP 64 Ry, are 0.54, 0.68, and 0.54 bohr; 1.11, 1.26, and 2.72 bohr; and 2.01, 2.01, and 2.72 bohr, respectively.